

Late-time evolution of nonlinear gravitational collapse

Lior M. Burko and Amos Ori

Department of Physics, Technion—Israel Institute of Technology, 32000 Haifa, Israel.

(April 14, 2018)

We study numerically the fully nonlinear gravitational collapse of a self-gravitating, minimally-coupled, massless scalar field in spherical symmetry. Our numerical code is based on double-null coordinates and on free evolution of the metric functions: The evolution equations are integrated numerically, whereas the constraint equations are only monitored. The numerical code is stable (unlike recent claims) and second-order accurate. We use this code to study the late-time asymptotic behavior at fixed r (outside the black hole), along the event horizon, and along future null infinity. In all three asymptotic regions we find that, after the decay of the quasi-normal modes, the perturbations are dominated by inverse power-law tails. The corresponding power indices agree with the integer values predicted by linearized theory. We also study the case of a charged black hole nonlinearly perturbed by a (neutral) self-gravitating scalar field, and find the same type of behavior—i.e., quasi-normal modes followed by inverse power-law tails, with the same indices as in the uncharged case.

PACS number(s): 04.70.Bw, 04.25.Dm

I. INTRODUCTION

The no-hair theorems state that except for the mass, the electric charge, and the angular momentum, all the features of fields which collapse to a black hole will be unobservable to external observers at late times. It is therefore interesting to study the mechanism by which the hair is radiated away (or absorbed by the black hole).

Until recently, the late-time evolution of non-spherical gravitational collapse was investigated primarily in the context of linear theory. That is, the deviations from spherical symmetry were considered as infinitesimally-small perturbations over a fixed curved background. The late-time behavior of such perturbations has been studied for three different asymptotic regions: (a) at fixed r , (b) along null infinity, and (c) along the future event horizon (when the collapse is to a black hole). Qualitatively, the evolution of the linearized perturbations is similar in these three asymptotic regions: During the first stage, the perturbations' shape depends strongly on the shape of the initial data. This stage is followed by the stage of quasi-normal (QN) ringing, in which the perturbations oscillate with an exponentially-decaying amplitude. The corresponding complex frequency is characteristic of the parameters of the background black-hole, and is independent of the details of the initial perturbation. Finally, there are also 'tails', characterized by an inverse power-law decay.

The asymptotic region (a) was first studied by Price [1], who analyzed the linear perturbations over a fixed Schwarzschild background. Price found that after the QN ringings die out, the perturbations at fixed r (outside the black hole) decay according to $t^{-(2l+\mu+1)}$, where $\mu = 1$ if there were an initial static mode, and $\mu = 2$ otherwise. Here, l is the multipole moment of the mode in question,

and t is the standard external Schwarzschild time coordinate. Asymptotic regions (b) and (c) were considered by Gundlach, Price and Pullin [2], who showed that the tails along null infinity decay according to $u_e^{-(l+\mu)}$, where u_e is the outgoing Eddington-Finkelstein null coordinate. (Hereafter we use the notation u_e and v_e for the outgoing and ingoing Eddington-Finkelstein null coordinates, correspondingly, in order to distinguish them from other types of null coordinates which we use later.) Along the event horizon (EH), the inverse-power indices were found to be similar to the asymptotic limit (a); Namely, the 'tails' decay according to $v_e^{-(2l+\mu+1)}$.

Recently, Krivan, Laguna and Papadopoulos studied numerically the evolution of linearized scalar-field [3] and spin-2 perturbations [4] over a fixed Kerr background. (See also [5].) They concluded that 'tails' are expected also for the Kerr background, with power-law indices similar to those obtained for Schwarzschild. This provides additional motivation for the study of the fully-nonlinear evolution of perturbations in the spherically-symmetric case as a toy-model for the spinning case, since the spherical case is much simpler to deal with (both analytically and numerically).

The numerical simulation of the fully-nonlinear gravitational collapse of a spherically-symmetric self-gravitating scalar field was recently carried out by two groups: Gundlach, Price and Pullin [6] (GPP), and Marsa and Choptuik (MC) [7]. In both analyses, the coordinates used were non-vacuum generalizations of the (one null+ r) outgoing [6] or ingoing [7] Eddington-Finkelstein coordinates. These numerical analyses demonstrated the QN ringing as well as the power-law 'tails' for lines $r = \text{const}$. In addition, MC also demonstrated the power-law decay at the EH.

In this paper, too, we study the nonlinear spherical

gravitational collapse of a self-gravitating scalar field. However, we shall use different coordinates, different numerical methods, and a somewhat different model. Our numerical code is stable and second-order accurate and is based on free evolution and double-null coordinates. This combination has several advantages: First, the null coordinates are very well adapted to the hyperbolic character of the field equations evolved: The evolution is along the characteristics, and consequently there is no restriction analogous to the Courant condition. Second, in double-null coordinates the interpretation of the causal structure of the numerically-produced spacetime is trivial. Also, double-null coordinates can be chosen such that the metric is regular at the EH, which is not the case in outgoing Eddington-Finkelstein coordinates.

Our coordinates and integration scheme allow us to study the evolution to arbitrarily late times, and there is no need to introduce an artificial outer boundary [7]. Our analysis demonstrates both the QN ringing and the power-law tails. One of our main objectives in this investigation is to numerically determine the power-law indices of the late-time tails in the nonlinear collapse problem, and to compare them to the predictions of the linear perturbation theory. In cases (a) and (c), we obtained power-law indices similar to those found by [6,7], though with improved accuracy. In addition, we obtain the power-law index at null infinity, which was not studied so far in nonlinear collapse. In all three asymptotic limits, we find an excellent agreement between our numerically-obtained indices and the values predicted by the linear perturbation analyses [1,2]. (Such an agreement is expected, even in a very nonlinear collapse problem, because of the “no-hair” principle—see e.g. Ref. [6].)

Whereas this paper considers only the external part of the black hole, we are currently investigating the inner structure of charged black holes with a similar numerical code [8]. In fact, our main motivation in this project is to develop the numerical approach and techniques which could later be used in investigating the black hole’s interior. The determination of the correct late-time power-law index is essential for that purpose.

Similar self-gravitating collapse scenarios have been recently used for the study of critical phenomena in black hole formation [9–11]. At its present form our code is incapable of treating these phenomena because we have not attempted to include the neighborhood of the origin in the domain of integration. The configurations we are interested in here are by far super-critical, and the aspects which concern us do not require the integration near the origin (see below).

This paper is organized as follows: In Section II we present the model for the collapse, and the corresponding field equations. Section III describes the numerical approach, and Section IV discusses the stability and accuracy of our code, and the tests used to verify them. It

has been recently argued [12] that unconstrained codes in double-null coordinates suffer from inherent instabilities. We show that this is not the case, and that our code is indeed stable and converges with second order. (In the Appendix we explain this in greater detail.) In Section V we present our numerical results for the collapse of a scalar field over a Minkowski background, leading to the formation of a Schwarzschild black hole, and in Section VI we consider the collapse of a (self-gravitating, neutral) scalar field on a RN background. Finally, in section VII we summarize and discuss our results.

II. THE COLLAPSE MODEL

A. The field equations

We shall consider the spherically-symmetric gravitational collapse of a self-gravitating, minimally-coupled, massless scalar field. In the uncharged case, the system is described by the coupled Einstein-Klein-Gordon field equations. We shall also consider the charged case, i.e. the case in which a (source-less) spherically-symmetric electric field is also present. In this case, the system is described by the coupled Einstein-Maxwell-Klein-Gordon field equations.

We write the field equations in double-null coordinates. The line element takes the form

$$ds^2 = -f(u, v) du dv + r^2(u, v) d\Omega^2, \quad (1)$$

where $d\Omega^2$ is the line element on the unit two-sphere. The general spherically-symmetric solution of the Maxwell equations in these coordinates is

$$F_{uv} = -F_{vu} = \frac{1}{2} \frac{Qf}{r^2} \quad (2)$$

and $F_{\mu\nu} = 0$ otherwise, where Q is a free parameter, which is interpreted as the electric charge, and where $F_{\mu\nu}$ is the Maxwell field tensor. The contribution of this electric field to the energy-momentum tensor is

$$T_{\mu\nu}^{\text{em}} = \frac{Q^2}{8\pi r^4} \begin{pmatrix} 0 & f/2 & 0 & 0 \\ f/2 & 0 & 0 & 0 \\ 0 & 0 & r^2 & 0 \\ 0 & 0 & 0 & r^2 \sin^2 \theta \end{pmatrix}. \quad (3)$$

The energy-momentum tensor of a massless scalar field Φ is

$$T_{\mu\nu}^{\text{s}} = \frac{1}{4\pi} \left(\Phi_{,\mu} \Phi_{,\nu} - \frac{1}{2} g_{\mu\nu} g^{\alpha\beta} \Phi_{,\alpha} \Phi_{,\beta} \right). \quad (4)$$

This field satisfies the Klein-Gordon equation $\Phi_{;\alpha}{}^{;\alpha} = 0$, which, in our coordinates, takes the form

$$\Phi_{,uv} + \frac{1}{r} (r_{,u} \Phi_{,v} + r_{,v} \Phi_{,u}) = 0. \quad (5)$$

The Einstein field equations are $G_{\mu\nu} = 8\pi T_{\mu\nu}$, where the energy-momentum tensor is the sum of the contributions of both the electromagnetic and scalar fields, $T_{\mu\nu} = T_{\mu\nu}^s + T_{\mu\nu}^{\text{em}}$. These equations include two evolution equations,

$$r_{,uv} = -\frac{r_{,u}r_{,v}}{r} - \frac{f}{4r} \left(1 - \frac{Q^2}{r^2}\right) \quad (6)$$

and

$$f_{,uv} = \frac{f_{,u}f_{,v}}{f} + f \left\{ \frac{1}{2r^2} [4r_{,u}r_{,v} + f \left(1 - 2\frac{Q^2}{r^2}\right)] - 2\Phi_{,u}\Phi_{,v} \right\}, \quad (7)$$

supplemented by two constraint equations:

$$r_{,uu} - (\ln f)_{,u}r_{,u} + r(\Phi_{,u})^2 = 0 \quad (8)$$

$$r_{,vv} - (\ln f)_{,v}r_{,v} + r(\Phi_{,v})^2 = 0. \quad (9)$$

The constraint equations are not independent of the dynamical equations: Any solution of the evolution equations will also be a solution of the constraint equations, provided only that the latter are satisfied on the initial hypersurface. (This is assured by virtue of the contracted Bianchi identities.)

B. The formulation of the characteristic problem

In our numerical scheme, we shall use the three equations (5)–(7) to evolve the three unknowns $r(u, v)$, $f(u, v)$, and $\Phi(u, v)$. These equations form a hyperbolic system, and thus ensure a well-posed initial-value formulation. In the double-null coordinates we use, it is most natural to use the characteristic initial-value formulation, in which the initial values of the unknowns (but not of their derivatives) are specified on two null segments, $u = \text{const} \equiv u_i$ and $v = \text{const} \equiv v_i$.

In such a numerical scheme (often called *free evolution*), the constraint equations are only imposed on the initial hypersurfaces. As mentioned above, the consistency of the evolving fields with the constraint equations is mathematically guaranteed. We use the constraint equations to check the accuracy of the numerical simulation.

From the pure initial-value viewpoint, we need to specify three initial functions on each segment of the initial surface: r , f , and Φ . The constraint equations, however, reduce this number by one: Eq. (8) imposes one constraint on the initial data at $v = v_i$, and similarly, Eq. (9) imposes one constraint on the initial data at $u = u_i$. The remaining two initial functions, however, represent only *one* physical degree of freedom: The other

degree of freedom expresses nothing but the gauge freedom associated with the arbitrary coordinate transformation $u \rightarrow \tilde{u}(u)$, $v \rightarrow \tilde{v}(v)$ (the line element (1) and all the above equations are invariant to this transformation). In what follows we shall use a standard gauge, in which r is linear with v or u , correspondingly, on the two initial null segments. On the outgoing segment we take $r_{,v} = 1$. On the ingoing segment, we take $r_{,u} = \text{const} \equiv r_{u0}$. The initial values of r are thus uniquely determined by the parameter $r_0 \equiv r(u_i, v_i)$. We choose $u_i = 0$ and $v_i = r_0$, and thus we find:

$$r_v(v) = v, \quad r_u(u) = r_0 + ur_{u0}.$$

(Hereafter, we denote the initial values of the three fields on the two initial segments by $r_u(u)$, $f_u(u)$, $\Phi_u(u)$ and $r_v(v)$, $f_v(v)$, $\Phi_v(v)$, correspondingly.) Then, we can freely specify $\Phi_u(u)$ and $\Phi_v(v)$ (this choice represents a true physical degree of freedom). The initial value of f is now determined from the constraint equations, namely

$$(\ln f_u)_{,u} = r_u(\Phi_{u,u})^2/r_{u0}, \quad (\ln f_v)_{,v} = r_v(\Phi_{v,v})^2, \quad (10)$$

together with the choice $f(u_i, v_i) = 1$. Thus, in the gauge we use, the geometry in the entire domain of dependence is uniquely determined by the two initial functions $\Phi_u(u)$ and $\Phi_v(v)$, and the two parameters r_0 and r_{u0} . (Later we shall relate r_{u0} to the initial black-hole mass.) In what follows, we shall consider initial data corresponding to a compact ingoing scalar-field pulse, over a background of either Minkowski, Schwarzschild, or RN. Namely, we shall assume that $\Phi_u(u) \equiv 0$; and Φ_v is also zero, except at a finite interval $v_1 < v < v_2$ (with some $v_1 \geq v_i$) where $\Phi_v \neq 0$. For concreteness, in the range $v_1 < v < v_2$ we shall take $\Phi_v = A \sin^2[\pi(v - v_1)/(v_2 - v_1)]$. This choice for the initial data is smooth at the matching points $v = v_1$ and $v = v_2$. The determination of $f_v(v)$ throughout $u = u_i$, by analytically integrating the second constraint equation in (10), is straightforward for such a pulse. On the ingoing segment $v = v_i$ we have $f_u(u) = 1$.

The geometry is static (with $\Phi = 0$) in the entire range $v < v_1$, with a mass parameter M_0 . To relate M_0 to the above initial-value parameters, we define the mass-function $M(u, v)$ [13] by $r_{,\mu}r^{,\mu} = 1 - 2M(u, v)/r + Q^2/r^2$. In our coordinates this becomes

$$M(u, v) = (r/2)(1 + 4f^{-1}r_{,u}r_{,v}) + Q^2/2r, \quad (11)$$

which yields $M_0 = (r_0/2)(1 + 4r_{u0}) + Q^2/2r_0$. Thus, our initial-value set-up is determined by the initial mass-parameter M_0 , the charge Q , and the perturbation amplitude A (together with the auxiliary parameters v_1 , v_2 and r_0).

We shall particularly study two cases: (i) $M_0 = 0$, $Q = 0$ (Minkowski background), and (ii) $M_0 = 1$, $Q \neq 0$ (RN background). [Note that no loss of generality is caused by the choice $M_0 = 1$, because of the scale-invariance nature of the problem.] We shall not elaborate here on the

situation of self-gravitating scalar field collapsing over a Schwarzschild background, as its outcome is qualitatively similar to case (i) (and, the collapse over Minkowski brings out the nonlinear aspects in a sharper way). We shall use, however, the pure ($A = 0$) Schwarzschild case as a test-bed for our numerical code.

In what follows, we shall use the symbols u and v to denote the outgoing and ingoing null coordinates in the specific gauge described above. Notice that v is closely related to v_e at $v \gg M$, and u is Kruskal-like near the EH (namely, it regularizes the metric function f at the EH).

The double-null line element suffers from a non-physical coordinate singularity at the origin (i.e., the timelike worldline $r = 0$, where the geometry is perfectly regular). This singularity may cause difficulties in the numerical study of case (i) above (i.e., Minkowski background). In order to overcome this difficulty, we restrict the domain of numerical integration in this case such that it will not include the origin. That is, the characteristic initial segment $v = v_i$ ends before it reaches $r = 0$. Since it is very essential that the domain of integration will include the EH, we must demand that the ingoing ray $v = v_i$ will intersect the EH before it intersects $r = 0$. This is achieved if the amplitude parameter A is sufficiently large.

III. THE NUMERICAL CODE

Our numerical code is based on the standard procedure for second-order integration of (1+1) hyperbolic equations in double-null coordinates: Let du and dv be the finite increments in the u and v directions, respectively. Let us also denote schematically the three unknowns r, f, Φ as h_i , $i = 1, 3$; These unknowns satisfy a field equation of the form

$$h_{i,uv} = F_i(h_j, h_{j,u}, h_{j,v}), \quad j = 1, 3. \quad (12)$$

Assume now that we already know the values of h_i at the three grid points $p_1 \equiv (u_0, v_0)$, $p_2 \equiv (u_0 + du, v_0)$, and $p_3 \equiv (u_0, v_0 + dv)$, and we would like to evaluate them at $p_4 \equiv (u_0 + du, v_0 + dv)$. We then use the substitution

$$h_i^{(4)} = -h_i^{(1)} + h_i^{(2)} + h_i^{(3)} + F_i^{(5)} du dv, \quad (13)$$

where, for any function g , $g^{(k)} \equiv g(p_k)$, and p_5 is the intermediate point: $p_5 \equiv (u_0 + du/2, v_0 + dv/2)$. In order to evaluate the functions $h_j^{(5)}, h_{j,u}^{(5)}, h_{j,v}^{(5)}$ (required for the determination of $F_i^{(5)}$) to the desired accuracy, we use the standard “predictor-corrector” method. This procedure results in a second-order accuracy. With this method, we first calculate h_i along the ingoing ray $v = v_i + dv$ —starting at $u = u_i + du$, then solving for $u = u_i + 2du$, and so on, until the last grid point at $u = u_f$; Then we

turn to the next ingoing ray $v = v_i + 2dv$, and solve for all grid points along this ray; By this way we solve, ray after ray, until we cover the entire domain of integration, $v_i < v < v_f$, $u_i < u < u_f$. The accuracy is controlled by the global grid parameter N , which is the (initial) number of points per a unit interval in both the v and u directions. Typically we used $N = 10, 20$ or 40 , though in certain cases we also used the values $5, 80$, and 160 .

As long as our domain of numerical integration does not include the EH, this numerical scheme can be used with a fixed grid without any difficulties. When the EH is included, however, we face a fundamental difficulty. For simplicity, assume at this stage that $\Phi = 0$ and the spacetime is Schwarzschild (though the same conceptual difficulty arises also in non-static spacetimes). Let us denote by u_h the value of our Kruskal-like coordinate u at the EH. Let u_0 be a grid value of u just near the EH, and let u_1 be the next grid point in u , i.e. $u_1 \equiv u_0 + du$. We define $\delta r(v) \equiv r(u_1, v) - r(u_0, v)$. Of course, for the validity of the numerical integration it is necessary that $\delta r \ll r$ —and we shall indeed select the grid parameter du sufficiently small so as to satisfy this requirement at the initial segment $v = v_i$. The problem is that, δr grows unboundedly and very rapidly with v . Thus, in terms of the Eddington-Finkelstein coordinate v_e , along the horizon $\delta r \propto \exp(v_e/4M)$ (because at the horizon of Schwarzschild, $r_{,u} \propto \exp(v_e/4M)$, and $\delta r(v) \cong r_{,u}(u_0, v) du$.) It is therefore obvious that a code based on a fixed du cannot be used here. One might attempt to use a numerical scheme in which du depends on u (but not on v) in such a way that it becomes extremely small at the EH. But this turns out to be impractical too, because of the extremely large exponential factor: Typically we need to integrate up to v_e values of at least a few hundreds times M (otherwise we cannot study the power-law tails with a sufficient accuracy). This would demand a value of du as small as, say, 10^{-100} near the EH, which is obviously impractical, due to the roundoff error and other reasons.

In order to overcome this difficulty, we must use a dynamical grid-refinement algorithm. A sophisticated dynamical refinement scheme was recently developed by Hamadé and Stewart [10], in order to analyze the critical behavior at the origin. For our purposes, however, it is sufficient to use a simpler refinement scheme, which we call *point splitting*: In certain values of v , we check the variations in r (and, in fact, in all h_i) between any two adjacent grid points. If the difference in r between such two points $p_1 = (u_0, v_0)$ and $p_2 \equiv (u_0 + du, v_0)$ is greater than some threshold value, we introduce an intermediate grid point $p'_2 \equiv (u_0 + du/2, v_0)$, and calculate the interpolated values of all unknowns h_i at that point. We can now use the above three-points integration scheme to calculate h_i at $p'_4 \equiv (u_0 + du/2, v_0 + dv)$ from the values of these fields at p_1, p'_2, p_3 (and, later, to calculate h_i at $p_4 \equiv (u_0 + du, v_0 + dv)$ according to the field values at

p'_2, p_2, p'_4). This numerical procedure functions very well in double-null coordinates, especially due to the following reasons: First, in the three-points integration scheme, $(p_1, p_2, p_3) \rightarrow p_4$, there is no reference to any grid points at $u < u_0$ or $u > u_0 + du$. Therefore, it does not matter whether the increments du are uniform or not. Second, in this scheme there is no restrictions on the ratio of du and dv .

In practice, we proceed as follows. We register all grid values of u (at a given v) in a vector $u(I)$, where I is an integer index. The values of the three unknowns are registered in corresponding three vectors $h_i(I)$. We define three threshold parameters h_i^c for the three unknowns, and also a “band parameter” v_b (typically we take v_b to be of order M). At the end of each interval v_b in v (a “band”), we check the variation of all three fields along the vectors $h_i(I)$. If for a given I the relative difference $|[h_i(I+1) - h_i(I)]/h_i(I)|$ is found to be greater than h_i^c (for any i), then we add a new grid point at $u = [u(I) + u(I+1)]/2$. In such a case, we calculate the values of the fields h_i at that new point by interpolation (usually we perform a four-points interpolation, based on, e.g., $u(I-1), u(I), u(I+1), u(I+2)$). We now update the vectors $u(I)$ and $h_i(I)$, by assigning the value $I+1$ to the new grid point. (Before creating this new grid point, we arrange an empty “slot” for it, by shifting all grid index values $I' > I$ by one.) The threshold values h_i^c are taken to be proportional to $1/N$, in order to preserve the rule of N as a parameter that controls the global accuracy (that is, the number of grid points in the u axis should be proportional to N). The band parameter v_b is taken to be independent of N .

Because our goal is to study the evolution in the entire black-hole exterior, the domain of integration must include the EH and thus extend into the black hole (i.e., $u_f > u_h$). Then, if $Q = 0$, the numerical integration will terminate at some finite v , beyond which the ingoing null lines $v = \text{const}$ intersect the spacelike $r = 0$ singularity (before $u = u_f$). In order to overcome this difficulty, we simply chop the vector $u(I)$ just beyond the apparent horizon (AH). Namely, at the end of each band, we first find I_{AH} , the value of the index I where the AH is located. This is the value of I satisfying $r_{,v}(u = u(I-1)) > 0$ and $r_{,v}(u = u(I)) < 0$.* We then chop the vector $u(I)$ at, say, $I = I_{AH} + 1$. This ensures that the domain of integration never gets close to the spacelike $r = 0$ singularity—and yet it contains the entire external part of the domain $v_i < v < v_f$, $u_i < u < u_f$,

up to (and including) the EH.

With these procedures of point-splitting and chopping, our code can in principle run to arbitrarily large v values. Due to point-splitting, however, the number of grid points in the vector $u(I)$ grows linearly with v_e , so the integration time grows like v_e^2 . In order to significantly decrease this time, we introduce two additional types of numerical manipulations:

point removal: The successive addition of points near the event horizon results in a coverage of the regions $r \gg 2M, v_e \gg M$ with an approximately uniform density of order N points per unit u_e (Recall that a point added at u just before the EH will, after an interval $v_e \gg M$, approach $r \gg 2M$.) However, for an appropriate coverage of the variations in r , a much smaller density of about NM/r points per unit u_e will be sufficient (note that at $r \gg 2M$, r is approximately linear in u_e along lines $v = \text{const}$). Thus, in order to save integration time, at the end of each band we check along the vector $u(I)$ and simply remove all unnecessary points, thereby shortening this vector. The criterion for necessity or otherwise of a point I is qualitatively similar to that of point-splitting: Again, we define the threshold values h_i^c for point removal (typically, h_i^c is slightly smaller than $h_i^c/2$). If for all i we have $|[h_i(I-1) - h_i(I)]/h_i(I)| < h_i^c$, then the point I is removed[†].

gauge correction: As it turns out, for any Kruskal-like u (which is necessary for a regular coverage of the EH) and Eddington-like v , f grows exponentially with v_e along the EH. In addition, along lines $v = \text{const} \gg M$, f grows rapidly (exponentially with u_e) in most of the interval $u_i < u < u_h$. The above numerical scheme handles very well this behavior of f . However, the significant variation of f with u implies that points can hardly be removed, which results in a long computation time. In order to overcome this difficulty, we introduce (as an option) a gauge correction at the end of each “band.” That is, we perform a coordinate transformation $u \rightarrow u_{\text{new}}(u)$. The value of f is gauged accordingly: $f_{\text{new}} = (du_{\text{old}}/du_{\text{new}})f_{\text{old}}$ (the variable r is unchanged). Our field equations are invariant to such a coordinate transformation. The function $u_{\text{new}}(u)$ is to be chosen so as to decrease the variation of f_{new} with u . A convenient choice is to take $u_{\text{new}}(u, v_0) = r(u, v_0)$ (where v_0 is the value of v at the ingoing ray where the gauge transformation is carried out), in which case f_{new} turns out to be approximately constant throughout the ingoing ray. (Another convenient choice is to

* We also calculate u_{AH} by interpolating between the two points $u(I-1)$ and $u(I)$. (In the Schwarzschild or RN cases $u_{AH} \equiv u_h$, but in the general dynamic case $u_{AH} \geq u_h$. Recall that only the AH can be found locally. However, for large v the AH should coincide with the EH.)

[†]In fact, the criterion we use for the variation in Φ (for both point-splitting and point removal) is somewhat more involved: It refers to the variations in both Φ and $\Phi_{,u}$. This is essential for the appropriate coverage of the maxima and minima regions in the QN ringing.

define $u_{new}(u)$ by the demand $f_{new}(u, v_0) = 1$.) We recall, however, that our goal is to numerically compute $f_{original}$ (as well as r and Φ) as a function of $u_{original}$ and v , and the gauge transformations are just a subsidiary manipulation. In order to accomplish this goal, we must keep record of two additional variables: (i) the vector $u_{original}(I)$, and (ii) the vector $R_g(I)$, where $R_g \equiv du_{current}/du_{original}$ is the cumulative gauge factor. At each gauge transformation, the latter is updated according to $R_{g(new)} = (du_{new}/du_{old})R_{g(old)}$. Consequently, in the original gauge the metric function f is given by $f_{original} = R_g f_{current}$.[‡] Hereafter, whenever we mention u and f , we refer to $u_{original}$ and $f_{original}$, correspondingly.

The combination of the above four types of numerical manipulations yields an accurate and efficient numerical code. It is important to recall that, whereas the *point-splitting* and *chopping* are necessary for an integration to large values of v , the *point removal* and *gauge correction* are optional, and are aimed to save integration time[§]. With these two manipulations, the typical number of grid points in the vector $u(I)$ grows only logarithmically with v_e , instead of linearly. In practice, the integration times in long runs are reduced by a factor of 10 or so. Typically, in a running to large v , almost all points in u are “born” in point-splitting near the EH, and are later removed when they approach $r \gg 2M$. We emphasize that in the numerical scheme described here the increment in v is fixed, $dv = 1/N$.

IV. STABILITY, ACCURACY, AND ERROR ANALYSIS

Stability

Gundlach and Pullin (GP) [12] recently argued that any free-evolution scheme will be inherently unstable, in

[‡] In a point-splitting, the variables $u_{original}(I)$ and $R_g(I)$ are interpolated at the point added, like the other variables $h_i(I)$.

[§] If a gauge-correction is not used for any reason, then, as a consequence of successive point-splittings, the difference in u between two adjacent points near the horizon becomes as small as, say, 10^{-100} . Then, due to the roundoff error, it is not possible to calculate $du(I) \equiv u(I+1) - u(I)$ directly at each step. One way to overcome this difficulty is to keep an independent vector $du(I)$, and to update it at every point-splitting by dividing $du(I)$ by two. (Recall that it is du that is involved in the finite-difference integration scheme, not u .) Another possibility is to shift u by a constant, e.g. at the end of each “band,” so as to assign the AH the value $u = 0$ — in this case $u(I+1) - u(I)$ can be calculated directly at each stage.

the sense that small violations of the constraint equations will grow exponentially with t along lines $r = \text{const}$ — even if the evolution equations are exactly satisfied. We disagree with the theoretical analysis and interpretation made by GP, for reasons explained in the Appendix. Also, our numerical tests did not indicate any such numerical instability. Certain entities exhibit an exponential growth, but these entities are not the ones that may be used as authentic error indicators; rather, the exponential growth we encountered is merely a reflection of the passive exponential growth exhibited by various gauge-dependent entities (e.g., r, u , for Kruskal-like u) along lines $r = \text{const}$ (or along the EH) in the Schwarzschild geometry. We discuss this issue extensively in the Appendix.

In our stability tests, we numerically reconstructed the Schwarzschild spacetime (as well as RN and other spacetimes) up to t values of many thousands times M , and with values of the grid-parameter N ranging from 5 to 160. In all these cases, we found a stable numerical evolution.

Accuracy checks and error analysis

We used several methods to test and monitor the accuracy of our numerical code: (i) Comparing the results obtained with different values of the grid-parameter N ; (ii) monitoring the discrepancy in the two constraint equations (8,9) (as explained above, our integration scheme does not involve these equations); (iii) numerically reproducing known exact solutions: The Minkowski solution, the vacuum Schwarzschild solution, the electro-vacuum RN solution, and the self-similar spherically symmetric scalar-field solution [15] for the Einstein-scalar field equations. In all these cases our code reproduced the exact solutions very well (we have compared the metric coefficients r, f and the mass function). All these tests indicated that the code is stable, and the numerical errors decrease like N^{-2} , as expected from a second-order code (see examples below).

We present here the results for the numerical reproduction of the Schwarzschild solution. (Similar results were obtained for the other above-mentioned tests.) We start with initial data corresponding to $M = 1$. The drift of M from its initial value may then be used as an error indicator. Figure 1 displays M as a function of t along a line $r = \text{const}$, Fig. 2 shows the drift of M as a function of v along the EH, and Fig. 3 shows M as a function of u_e along null infinity, for various N values. From these Figures it is apparent that the mass drift is linear with time, and decreases like N^{-2} , as expected. We also compared the mass function obtained from local differentiation [Eq. (11)] with the dynamical mass function which evolves according to the wave equation [13]

$$m_{,uv} = 2 \frac{r^3}{f} \Phi_{,u}^2 \Phi_{,v}^2 - r \left(1 - \frac{2m}{r} + \frac{Q^2}{r^2} \right) \Phi_{,u} \Phi_{,v}. \quad (14)$$

Both expressions for the mass function agree with each other (in the limit of large N).

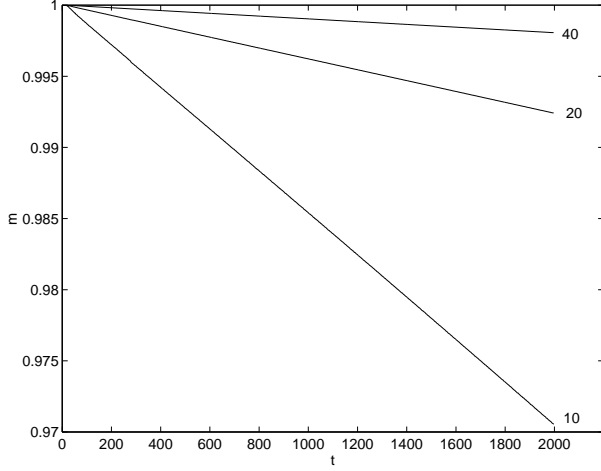


FIG. 1. The drift of the mass function along $r = \text{const}$. Shown here is the mass function as a function of t for $N = 10, 20$ and 40 . We took here $r = 8$.

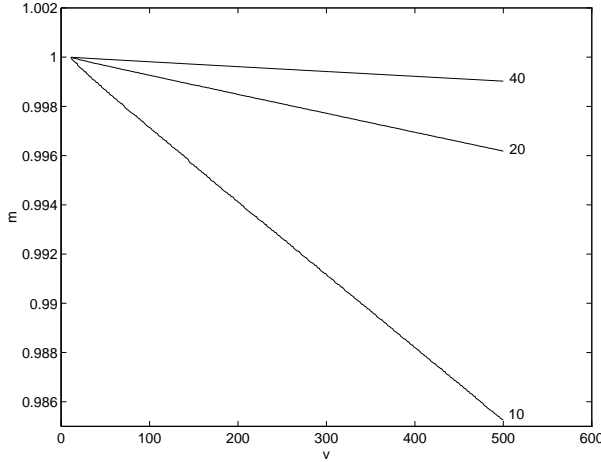


FIG. 2. The drift of the mass function along the EH, as a function of v , for $N = 10, 20$ and 40 .

Another check we performed was to compare the values of f as a function of t along lines $r = \text{const}$ of the numerically reproduced Schwarzschild spacetime and the exact analytical counterpart [16]. Figure 4 displays the results we obtained for $r = 3M$. (Similar behavior was found for other values of r .) It is convenient to compare the values of f in the outgoing Kruskal coordinate U_k and the ingoing Eddington coordinate v_e . For the Schwarzschild solution one finds that $g_{U_k v_e} = \frac{4M^2}{r} e^{-r/(2M)} e^{v_e/(4M)}$. Figure 4 shows the ratio F between $g_{U_k v_e}$ for the exact Schwarzschild solution and $g_{U_k v_e}$ in the numerically reproduced spacetime, along $r = 3M$, vs. the ingoing coordinate v , for several values of the grid parameter N .

This figure clearly indicates the second-order convergence of the code to the correct theoretical value.

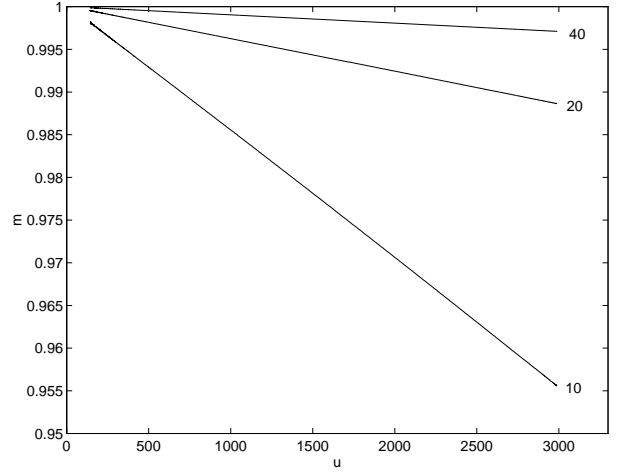


FIG. 3. The drift of the mass function along null infinity, as a function of u_e (calibrated such that $u_e = 0$ on $u = 0$), for $N = 10, 20$ and 40 .

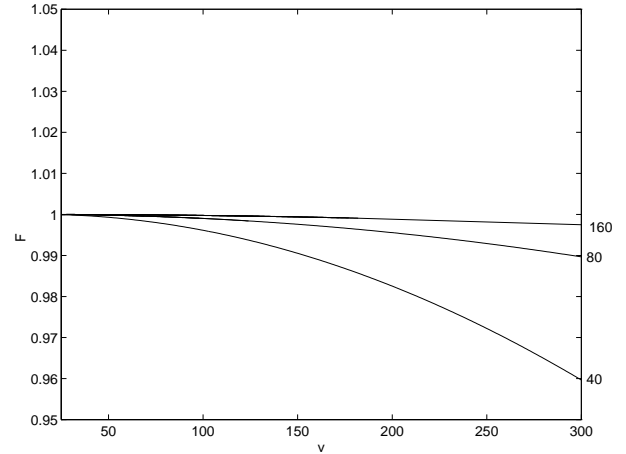


FIG. 4. The ratio F of $g_{U_k v_e}$ of the exact Schwarzschild solution and $g_{U_k v_e}$ of the numerically reproduced spacetime. Shown are the values for $N = 40, 80$, and 160 . The convergence indicates a second-order code. The deviation of the curves from straight lines results primarily from the linear drift of M .

As we mentioned above, we also use the constraint equations to monitor the errors. Let us denote the entities in the left-hand side of Eqs. (8,9) by C'_u and C'_v , respectively. Now, as they stand, C'_u and C'_v cannot be used as measures of the intrinsic local error in the reproduced spacetime, because they are not gauge invariant. Instead, whenever $r_{,u}$ or $r_{,v}$ are non-vanishing, we may define

$$C_u \equiv C'_{u,r^2_{,u}}, \quad C_v \equiv C'_{v,r^2_{,v}}.$$

Since C_u and C_v are gauge-invariant, they provide an invariant measure of the local numerical error. An alter-

native gauge-invariant indicator is $C \equiv f^{-1} (C'_u C'_v)^{1/2}$. Note that the indicator C_v cannot be used at the AH, where $r_{,v}$ vanishes. Instead, one may use the indicator C there. Figure 5 displays C_u and C_v at constant r as functions of t (we took here $r = 3$), and C_u and C at the EH, as functions of v . From Figure 5 one can see that these indicators are roughly constant with time. (The noise is a results of the second-order numerical differentiation necessary for the computation of the indicators.) In particular, no exponential growth occurs. This demonstrates the stability of the code. We found a similar behavior also for the electro-vacuum RN spacetime.

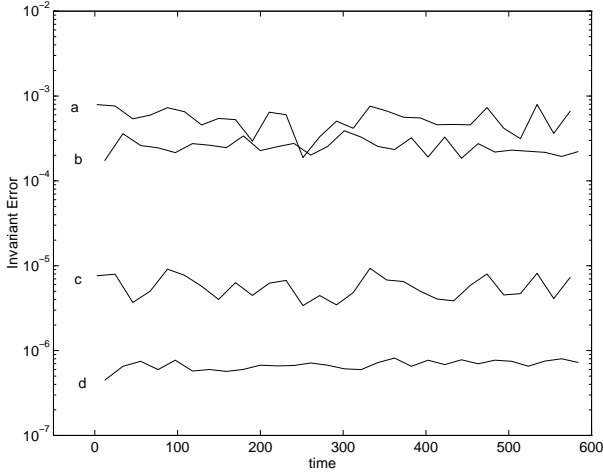


FIG. 5. The gauge-invariant error indicators $|C_u|$ and $|C_v|$ along a line $r = \text{const}$ as functions of t , and $|C_u|$ and $|C|$ along the EH as functions of v_e . Line a: $|C_u|$ along $r = \text{const}$, line b: $|C_u|$ along the EH, line c: $|C_v|$ along $r = \text{const}$, and line d: $|C|$ along the EH. The data are taken for $r = 3$ and $N = 40$.

Figure 6 shows the rate of convergence of various error indicators as N increases. The spacetime simulated here is RN with $Q/M = 0.8$. (The other exact solutions we checked produced similar results.) Shown are the l_p -norms, for several p values, of the two vectors made of the values of the indicators C_u and C_v , respectively, along a particular outgoing ray located before the EH. We used the following values of N : 5, 10, 20, 40, 80, and 160. The apparently straight lines in the logarithmic graphs indicate a second-order convergence**. (The break in the lines e and f for $N = 160$ seems to be a roundoff effect.) The other error indicators we used (e.g., the drift of the mass function and the metric functions) also indicated a second-order convergence rate.

**From the slopes of the curves displayed in Fig. 6 we can estimate the convergence rate of the code to be around 1.9, with variations of typical order 0.1. We stress, however, that these numbers would depend on the method employed for evaluating the convergence rate.

V. NON-LINEAR COLLAPSE ON MINKOWSKI

In this section we consider the case $M_0 = 0, Q = 0$, namely, the collapse of the self-gravitating scalar field over a Minkowski spacetime, leading to the formation of a Schwarzschild-like black hole. Our initial data correspond to a compact sinusoidal ingoing pulse, as described in Section II. Here, we take $v_1 = 6, v_2 = 16, r_0 = 6$, and $r_{u0} = -1/4$ (corresponding to $M_0 = 0$). The final mass of the black hole is then determined by the pulse amplitude A . In what follows we present the results of a numerical simulation with $A = 0.4$, leading to a final black-hole mass $M_f \cong 3.54$. (Hereafter, we denote by M_f the final mass of the black hole.)

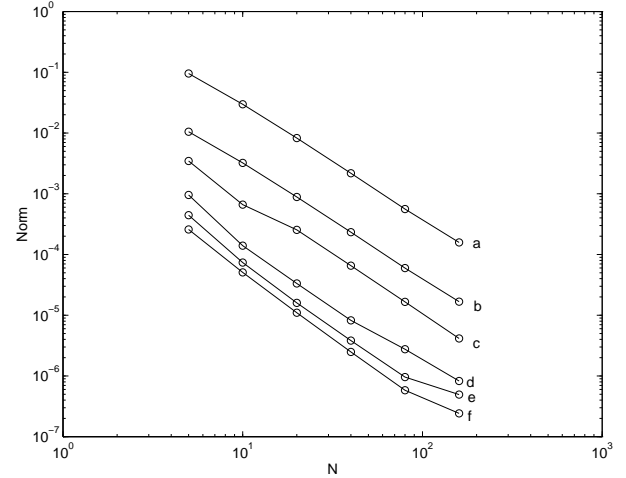


FIG. 6. The l_p -norms of the constraints C_u and C_v along an outgoing null ray, as functions of the grid parameter N . The cases a, b, and c refer to the l_1, l_2 , and l_∞ -norms, respectively, for C_u , and cases d, e, and f refer to the l_1, l_2 , and l_∞ -norms, respectively, for C_v . The numerical data are represented by circles, and the straight lines between the circles are linear interpolations of the data.

Figure 7 displays the Bondi mass of the created black hole as a function of the retarded time u_e .^{††} The Bondi mass decreases with u_e , due to the escape of scattered energy to null infinity. The late-time decrease of the mass corresponding to the power-law tail of the scattered scalar field is too small to be observed in this figure (the numerical drift shown in Fig. 3 is also unobservable in the scale used in Fig. 7).

The nonlinearity of the spacetime dynamics is best rep-

^{††}Strictly speaking, u_e is not well-defined here, as the spacetime is dynamical and differs from Schwarzschild. In the asymptotic region $r \gg M_f$, however, the geometry becomes asymptotically Minkowski, and we can define u_e with respect to this asymptotic region. Namely, along a ray $v = \text{const}$ in this range, u_e is linear with r .

resented by the evolution of the mass function along the AH (which is just twice the value of r there). Figure 8 shows this mass as a function of v . The mass function grows rapidly, until it approaches a saturation value. In this case, too, the mass-increase at late time due to the power-law tail, and the numerical mass drift, are unseen. The final black-hole mass can be deduced from either the flat large- v portion of the graph in Fig. 8 or the flat large- u_e portion in Fig. 7—these two numbers agree, as they should.

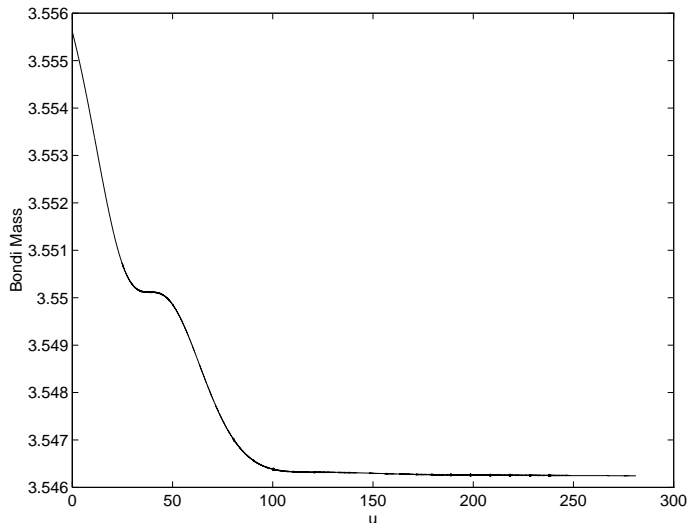


FIG. 7. The Bondi mass as a function of retarded time u_e (calibrated such that $u_e = 0$ on $u = 0$), for $N = 40$. The mass is displayed along the ingoing null ray $v = 10^6 M_f$, representing null infinity.

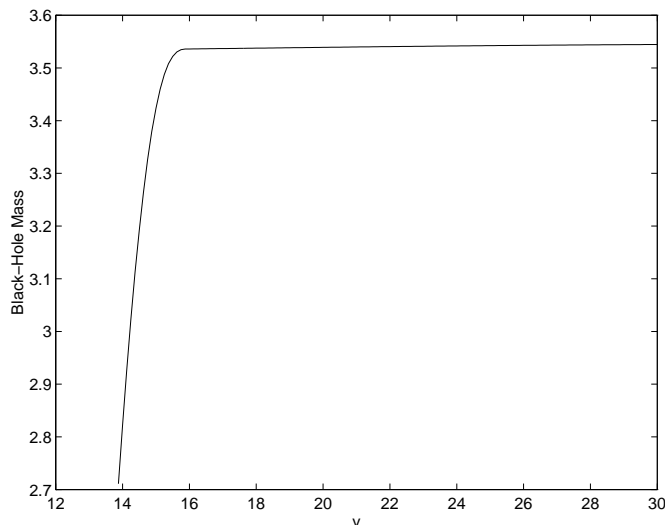


FIG. 8. Black-hole mass determined from the AH radius vs. v . At advanced times earlier than $v \approx 14$ the domain of integration, $u < u_f$, does not intersect the AH.

The stability and accuracy of our code is demonstrated in Fig. 9, which displays the scalar-field's QN ringing

along the horizon for $N = 5, 10, 20$, and 40: The four graphs are indistinguishable in this Figure. In addition, we also determined the QN ringing frequency, and compared it with the linear analysis value [17]. This comparison is hard, as we have only a few oscillations before the power-law tails start to dominate. In addition, the numerical mass drift (see above) complicates the comparison between the numerical results and the theoretical prediction. (However, the mass drift can be controlled by the grid parameter N . Note that the physical mass increase due to scalar-field absorption is negligible at late times.) From our numerical data we find that the QN frequency is $\sigma = 0.032 - 0.026 i$. The real part of σ was calculated from the two nodes in Fig. 9 corresponding to a full wavelength, and the imaginary part from the two local extrema between them. The theoretical value for the least damped mode with $l = 0$ is $\sigma_{th} = 0.031 - 0.029 i$ (recall that here $M_f \cong 3.54$). The sources for the deviation are the (numerical) drift in the mass, the effect of the other $l = 0$ modes and the power-law tails, and the inability to use values from many cycles. However, our numerically obtained value is remarkably close to the linear analysis value.

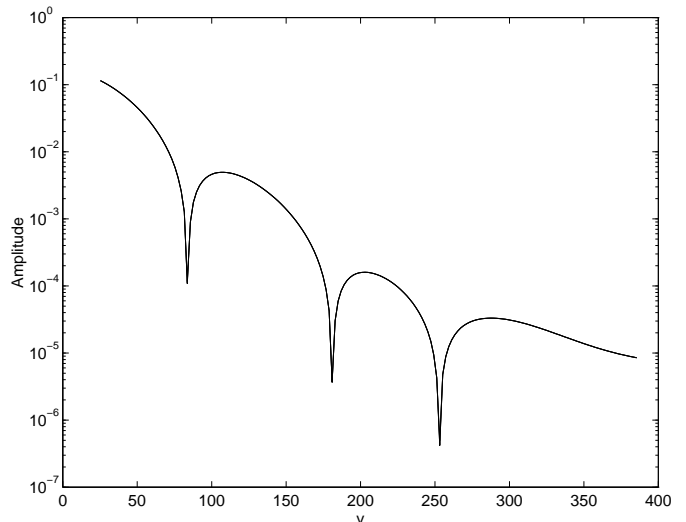


FIG. 9. Quasi-normal ringing at the horizon as a function of v_e . Recall that $M_f \approx 3.54$, which explains the relatively large value of v_e in which the ringing takes place. We used here four different values of N —5, 10, 20, and 40—but the four graphs are indistinguishable in this figure.

Figure 10 shows the late-time behavior of Φ in the three asymptotic regions: (a) – at fixed r , with $t \gg M_f$ (we take $t = (u_e + v_e)/2$), (b) – at future null infinity (represented here by $v_f = 10^6 M_f$), for $u_e \gg M_f$, and (c) – at the horizon, with $v \gg M_f$. This figure clearly demonstrates both the QN ringing and the power-law tails, in all three asymptotic regions.

The determination of the asymptotic behavior at null infinity poses a special difficulty: We cannot integrate up

to $v = \infty$ proper. (An attempt to compactify the coordinate v will not solve this problem, as it would lead to a divergence of f at null infinity.) We therefore represent null infinity by a large (but yet finite) value, $v = v_f$. This “null-infinity approximation” is only valid as long as $v_f \gg u_e$. Thus, the determination of the late-time behavior at null infinity clearly demands huge values of v_f , in order to satisfy $v_f \gg u_e \gg M_f$. In the simulations described in this paper, we used $v_f = 10^6 M_f$ to represent null infinity. In order to enable the integration to such large v values within a reasonable computation time, we used the following procedure: Let us denote by u_{ef} the maximal value of u_e in the desired presentation of the late-time null-infinity behavior (in Fig. 10, $u_{ef} = 10^4$). After integrating up to a value of v which corresponds to $v_e = u_{ef}$, we chop the vectors $u(I)$ and $h_i(I)$ at a value of u which corresponds to $u_e = u_{ef}$. The last point is now located at $r > 2M_f$. When we continue the integration to larger v values, the minimal value of r , $r_{min}(v) = r(u_e = u_{ef}, v)$, increases very rapidly and approaches large values (of order v). We can therefore increase dv accordingly, say, $dv(v) \approx r_{min}(v)/(10N)$. This allows us to integrate up to e.g., $v = 10^{10}$ within a very short integration time. (Practically, we change dv in discrete values of v , e.g. once in each decade.)

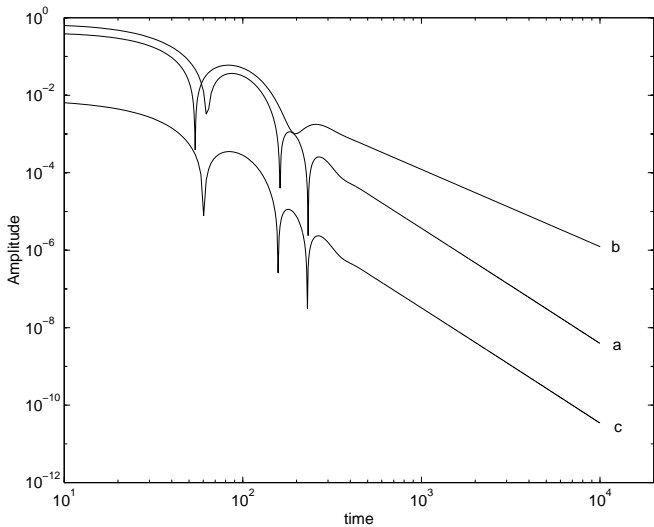


FIG. 10. The late-time behavior of the scalar field in the three limits (a),(b), and (c). Case (a): This graph displays Φ at $r = 2.3M_f$, as a function of t . Case (b): Φ along null infinity (represented by $v = 10^6 M_f$) versus retarded time u_e , calibrated such that $u_e = 0$ on $u = 0$. Case (c): Φ along the EH, as a function of v_e . (The amplitude in this case was divided by 100, so that it will not overlap with the other graphs). In all three cases, the QN ringing and the power-law tails are seen clearly. We used here $N = 20$.

As was mentioned above, one of our goals is to evaluate the power-law indices in the case of nonlinear collapse and to compare them to the predictions of the linear theory. Since our initial data correspond to $l = 0$ and to

zero initial static moment, the linear perturbation analysis would predict (negative) power indices 3, 2, and 3 in the cases (a), (b) and (c), correspondingly. In general, the slopes of the straight sections in the three graphs shown in Fig. 10 appear to agree with these predicted values. However, the standard best-fit method is not so useful in this case for a precise determination of the numerically-computed indices, due to the following reason. Consider, for example, the late-time behavior at the horizon. According to the linear theory, it should be dominated by v^{-3} . However, this dominant term is “contaminated” by higher-order terms in $1/v$, whose effect become larger as v decreases [18]. Assume now that we use the standard best-fit method (applied to a finite interval $v'_0 < v < v_f$) to determine the deviation of the power-law index from its predicted value. As it turns out, the computed deviation will be dominated in this case by the “higher-order contamination.” This contamination effect, in turn, will depend in an arbitrary way on the choice of the parameter v'_0 . In order to remove this arbitrariness, we introduce the notion of *local power index*, define by $-v\Phi_{,v}/\Phi$. (For the other asymptotic regions, v is to be replaced by t or u_e , accordingly.)

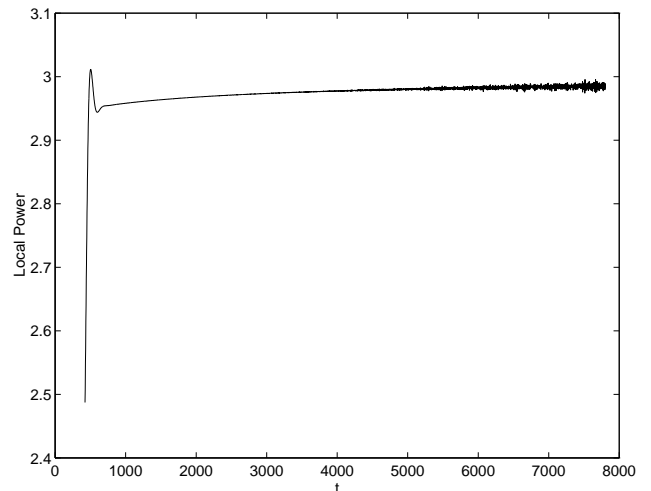


FIG. 11. Local index of the ‘tails’ for case (a): along $r = \text{const} = 2.3M_f$, as a function of t . The local power is 2.98 ± 0.01 . We used here $N = 20$.

The local power index for the three asymptotic regions is shown in Figs. 11, 12, and 13. The agreement with the predictions of linear theory is remarkable. In principle, deviations from the precise integer index may result from three sources of errors: (i) the limited accuracy of the numerical simulation; (ii) the finiteness of the late-time domain covered by the numerics, i.e. the finiteness of t , u , and v in Figs. 11, 12, and 13, correspondingly (due to the “higher-orders contamination”, the precise integer index is expected only at infinitely-late time); (iii) in case (b) (i.e. at null infinity), the finiteness of the final value $v =$

v_f taken to represent null infinity is also a possible source of error. In the numerical simulations presented here, we find that the deviation is related primarily to source (ii): We used a sufficiently large N , and a sufficiently large v_f in case (b), so sources (i) and (iii) are insignificant.

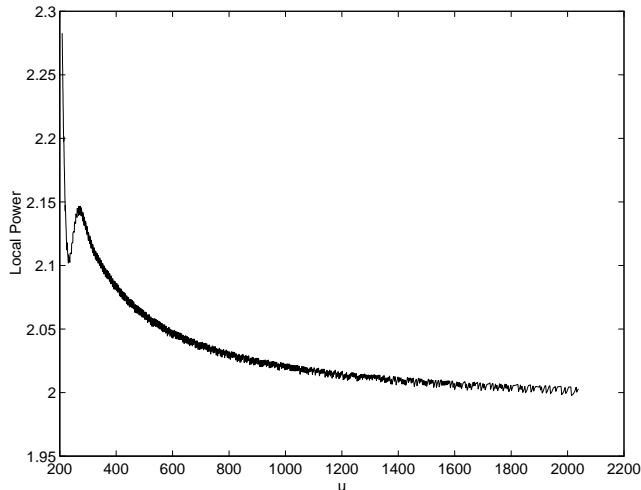


FIG. 12. Local index of the ‘tails’ for case (b): along $v = 10^6 M_f$ (representing future null infinity), as a function of u_e . The local power is 2.002 ± 0.003 . We used here $N = 20$.

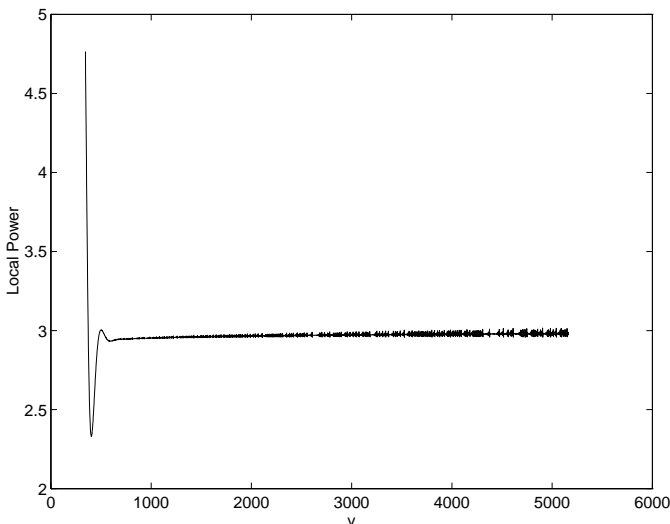


FIG. 13. Local index of the ‘tails’ for case (c): along the AH, as a function of v_e . The local power is 2.99 ± 0.02 . We used here $N = 20$.

Our results for the local index (at maximal t , u , or v) are:

- Case (a): 2.98 ± 0.01 (instead of 3),
- Case (b): 2.002 ± 0.003 (instead of 2),
- Case (c): 2.99 ± 0.02 (instead of 3).

The error bar represents the numerical “noise”, produced primarily by the numerical differentiation of Φ with respect to v , u , or t , which is inherent to the computation

of the local power index.

For comparison, we quote here the values obtained in previous nonlinear numerical analyses for the power-law indices. In case (a): 2.63–2.74 [6] and 3.38 [7]; in case (c): 3.06 [7]; No nonlinear results were obtained so far for case (b).

VI. NON-LINEAR COLLAPSE ON A CHARGED BACKGROUND

In order to study the nonlinear dynamics of charged black holes, we consider here the gravitational collapse of the self-gravitating (neutral) scalar field over a pre-existing charged background (a RN geometry). The model and initial-value set-up are as explained in Section II. We take here an initial mass $M_0 = 1$, and a charge $Q = 0.95$. (We found similar results for other values of $Q < 1$.) We now take $v_1 = 6, v_2 = 16, r_0 = 6$, and $r_{u0} \approx -0.1729$. As before, we take a scalar-field amplitude $A = 0.4$. The black-hole mass then increases to $M_f \cong 3.87$ during the collapse. Figure 14 shows the value of r at the AH vs. v . The rapid increase of the horizon’s area indicates strong nonlinear spacetime dynamics. The two-stage increase of r reflects the structure of the scalar-field pulse: The latter has a maximum at about $v = 11$, and the vanishing of $\Phi_{,v}$ implies $M_{,v} = 0$ there. (A similar behavior is observed in Fig. 7.)

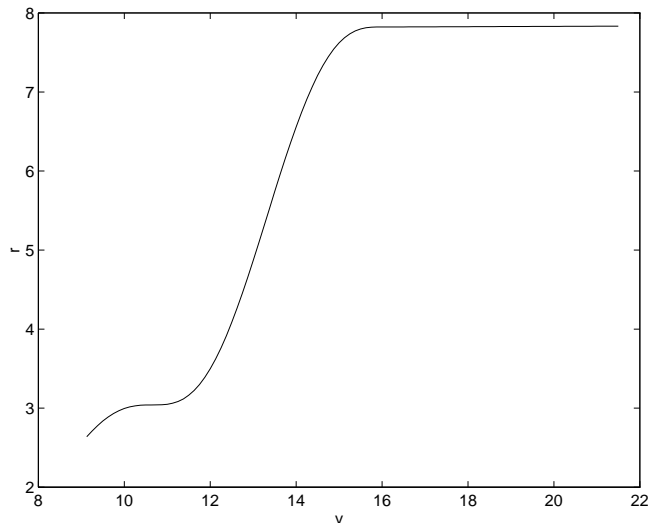


FIG. 14. Value of r at the AH as a function of v . (At early values of v our numerical domain of integration $u_i < u < u_f$ does not intersect the AH.) We used here $N = 20$.

According to the predictions of the linearized theory [14], the late-time behavior in the three asymptotic regions (a,b,c) in a (non-extreme) charged black hole should be similar to the uncharged case – namely, QN ringing followed by inverse power-law tails with the same indices as in the uncharged case. Figure 15 displays the

late-time behavior of the scalar field for the three asymptotic regions (a), (b), and (c). Again, both the QN ringing and the power-law tails are seen very clearly in all three asymptotic regions.

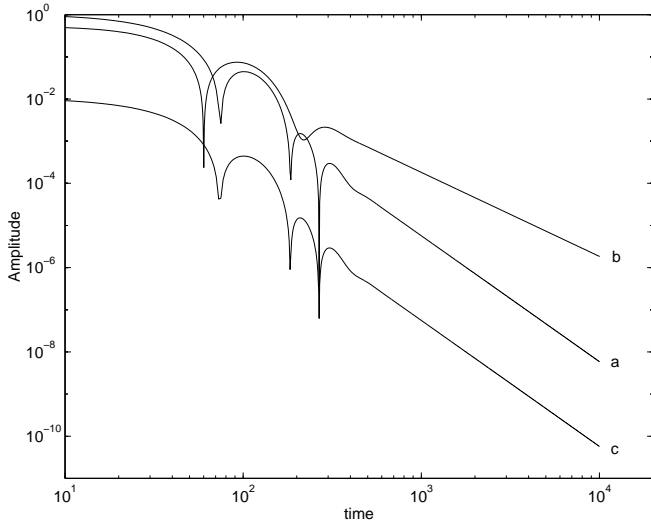


FIG. 15. Amplitude of the scalar field for the three cases (a), (b), and (c) for the nonlinear collapse on a charged RN background. Case (a): along $r = \text{const} = 2.3M_f$, as a function of t . Case (b): along $v = 10^6 M_f$, representing future null infinity, as a function of u_e (calibrated such that $u_e = 0$ on $u = 0$). Case (c): along the horizon, as a function of v_e . The amplitude for case (c) is divided by 100 to avoid overlap of the graphs. We used here $N = 20$.

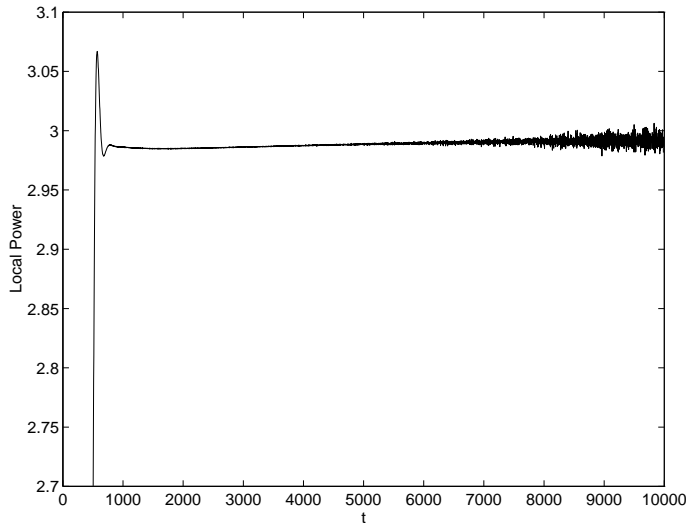


FIG. 16. Local power as a function of t for case (a): along constant value of r ($r = 2.3M_f$). The value of the local power approaches 2.99 ± 0.01 . We used here $N = 20$.

Figures 16, 17, and 18 show the local power index for the three asymptotic regions. Our results for the local power index (at maximal t , u , or v) are:

Case (a): 2.99 ± 0.01 (instead of 3),

Case (b): 1.996 ± 0.001 (instead of 2),

Case (c): 2.99 ± 0.02 (instead of 3).

These results are in excellent agreement with the predictions of the linear theory.

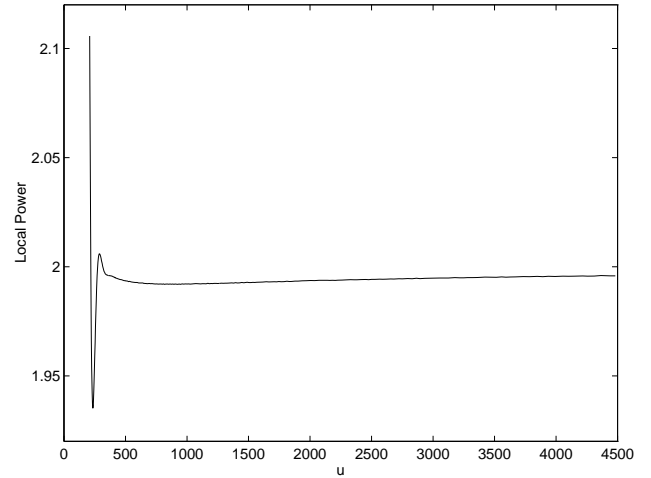


FIG. 17. Local power as a function of u_e for case (b): along future null infinity, represented by $v = 10^6 M_f$. The value of the local power approaches 1.996 ± 0.001 . We used here $N = 20$.

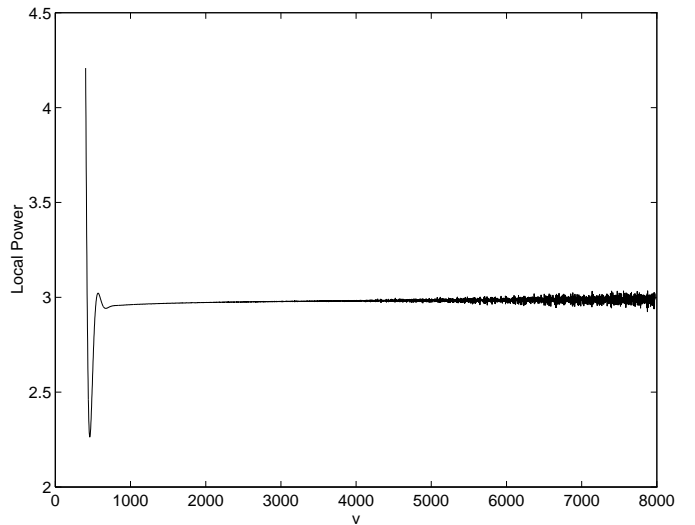


FIG. 18. Local power as a function of v_e for case (c): along the EH. The value of the local power approaches 2.99 ± 0.02 . We used here $N = 20$.

VII. CONCLUSIONS

We developed a numerical scheme for the integration of the spherically-symmetric nonlinear Einstein-Maxwell-Klein-Gordon field equations. Our scheme is based on free evolution in double-null coordinates. This scheme is stable and accurate, it is capable of running to arbitrarily

late times, and it can handle black holes while avoiding singularities.

We used this numerical code to study the gravitational collapse of a spherically-symmetric, self-gravitating, minimally-coupled scalar field to form a black hole (or the collapse of such a scalar field over a pre-existing charged background). Our numerical simulations demonstrate both the quasi-normal modes and the power-law tails, in all three late-time asymptotic regions: at a constant r (with large t), along future null infinity (at large u), and along the event horizon (at large v). The accuracy of our numerical scheme, its ability to run forever, and the method of calculating *local* power indices, allowed us to evaluate the power-law indices with an accuracy better than all previous estimates.

Our results confirm that the predictions of the linear theory for the late-time behavior of perturbations outside the black hole hold also for fully nonlinear collapse. (This observation is not surprising—in a sense, it is a manifestation of the principle that black holes have no hair.) In particular, in all three late-time asymptotic regions, the power-law indices approach asymptotically the integer values predicted by the linear perturbation analysis. This agreement of the late-time nonlinear dynamics and the linear perturbation theory was already demonstrated by GPP [6] in the uncharged case (see also [18]). Here we demonstrate it for the charged case as well.

The simulations presented here were restricted to the external part of the black hole and the neighborhood of the event horizon. One of our main motivations in this project, however, was to develop the numerical tools which will allow the investigation of the *inner* part of black holes. We are currently using this numerical scheme to study the evolution of the geometry and the scalar field near the spacetime singularity inside a charged black hole.

ACKNOWLEDGMENT

This research was supported in part by the Israeli Science Foundation administered by the Israel Academy of Sciences and Humanities.

APPENDIX A

At issue here is the evolution of the entities at the left-hand sides of Eqs. (8,9), which represent the violation of the constraint equations. These entities are denoted in Ref. [12] by E_1 and E_2 , respectively (in Section IV we denote these entities by C'_u and C'_v). GP argue that, as a consequence of the *precise* evolution equations, E_1 and E_2 will grow exponentially with t along lines $r = \text{const}$. According to GP, this exponential divergence represents an inevitable numerical instability of the free-evolution

scheme. We do not accept this conclusion, and claim that (i) under the precise evolution equations E_1 and E_2 do *not* grow exponentially; rather, they are essentially conserved (in a sense which will be explained below); (ii) in our numerical free-evolution scheme, E_1 (but not E_2) will grow exponentially, but this growth is a consequence of the *numerical error* in the integration of the evolution equations, not of the equations themselves. (iii) This divergence of E_1 does not indicate a numerical instability; Rather, it reflects the passive exponential growth of typical gauge-dependent entities like $r_{,u}$ along lines $r = \text{const}$ in the Schwarzschild geometry.

To verify point (i), assume that the evolution equations are precisely satisfied. Then, Eq. (7) in Ref. [12] reads $E_{1,v} = -(r_{,v}/r)E_1$. E_2 will satisfy an analogous equation: $E_{2,u} = -(r_{,u}/r)E_2$. It then follows that the entity rE_1 is conserved along lines $u = \text{const}$, and similarly rE_2 is conserved along lines $v = \text{const}$. Therefore, an exponential growth of E_1 or E_2 along lines $r = \text{const}$ is ruled out^{††}. The exponential divergence of the linear metric perturbations (denoted ξ and η in Ref. [12]) found by GP must therefore be a gauge mode. In fact, the infinitesimal coordinate transformation $u \rightarrow u + du$ (e.g., with fixed infinitesimal du) yields a nonvanishing ξ (in Ref. [12] ξ represents the linear perturbation in r^2), given by

$$\xi = -(r^2)_{,u} du = -2r r_{,u} du.$$

For any Kruskal-like u , at a fixed r , $r_{,u}$ grows like $\exp(t/4M)$ at $t \gg M$. It then follows that along any line $r = \text{const}$, at large t , ξ will exhibit this $\exp(t/4M)$ divergence. This fits very well with the rate of divergence, $\exp(0.24 t/M)$, found numerically by GP. But this is, of course, a gauge mode, which does not indicate a violation of the Einstein equations.

Note also that the analytic derivation of the exponential growth in Ref. [12] is based on the “mode ansatz” approximation. This approximation may only be valid if the mode’s wave-number k is sufficiently large. The diverging modes found by GP do *not* satisfy this condition, however. This may explain the discrepancy of the value $0.32 M^{-1}$ predicted by GP compared with the above theoretical value $1/(4M)$ (which is also confirmed numerically by GP to a good accuracy).

In our numerical tests, we found that along lines $r = \text{const}$, E_2 is roughly preserved, while E_1 grows like $\exp(t/2M)$. From the above discussion it is obvious that this exponential growth of E_1 must be a consequence

^{††} Such an exponential divergence would demand that, on the initial hypersurface, E_1 diverges exponentially with u_e , and E_2 diverges (almost) exponentially with v_e , which is an unreasonable situation.

of the *violation* of the evolution equations, due to numerical errors. Later we shall give a more explicit explanation for this behavior. The crucial point is, however, that the exponential growth of E_1 does not indicate an exponential growth of the intrinsic local error: The entity E_1 (like E_2) is not an appropriate error indicator, because it is not a gauge-invariant entity. [In a transformation $u \rightarrow u'(u)$, E_1 is multiplied by the factor $(du/du')^2$.] In order to extract from E_1 the information about the intrinsic local error, we must construct a gauge-invariant entity from it. A convenient choice is the gauge-invariant entity $C_u \equiv E_1/(r_{,u})^2$. This entity indeed remains roughly constant along lines $r = \text{const}$ and along the EH (see Fig. 5). The behavior of the other error indicators (e.g. the mass parameter in Figs. 1 and 2) also indicate stability: None of the invariant entities exhibit an exponential growth of error.

We still need to explain why the numerical errors in the integration of the evolution equations results in an exponential growth of E_1 . If there were no numerical errors in the integration, then, along a line $r = \text{const} \equiv r'$, E_1 would approach (at large t) a constant value, $E_1(u_h, v_i) r(u_h, v_i)/r'$. Correspondingly, C_u would decay like $1/(r_{,u})^2 \propto \exp(-t/2M)$. However, the numerical error in the integration of the evolution equations provide a (roughly) constant source of error in the evolution of C_u ^{§§}. The combination of the dynamical tendency to exponential decay and the constant source of error results in a finite saturation value (proportional to the numerical error)^{***}. In turn, this implies that E_1 grows like $\exp(t/2M)$.

Finally, we emphasize again that despite of the above discussion, whenever the domain of integration includes the EH, a naive attempt to use a free-evolution scheme in double-null coordinates, without a grid refinement, will inevitably result in a numerical instability due to the exponential divergence of $r_{,u}$ (see Section III). This might be the reason for the failure of previous attempts to use the free-evolution scheme. The grid refinement (in our case, the point-splitting procedure) is a necessary ingredient in such a numerical scheme.

^{§§} To understand why this source of error is roughly independent of t , recall that (i) in our integration scheme, due to the dynamical grid refinement, the intrinsic error production rate is essentially independent of t (or u), and (ii) C_u is an authentic indicator of the intrinsic local error.

^{***} Phenomenologically, we may represent the situation by the simple differential equation $dC_u/dt = -C_u/(2M) + S(r)$, where $S(r)$ is the numerical source term. C_u then approaches the asymptotic value $2MS(r)$.

- [1] R. H. Price, Phys. Rev. D **5**, 2419 (1972).
- [2] C. Gundlach, R. H. Price, and J. Pullin, Phys. Rev. D **49**, 883 (1994).
- [3] W. Krivan, P. Laguna, and P. Papadopoulos, Phys. Rev. D **54**, 4728 (1996).
- [4] W. Krivan, P. Laguna, and P. Papadopoulos, Report No. gr-qc/9701036 (unpublished).
- [5] W. Krivan, P. Laguna, P. Papadopoulos, and N. Andersson, Report No. gr-qc/9702048 (unpublished).
- [6] C. Gundlach, R. H. Price, and J. Pullin, Phys. Rev. D **49**, 890 (1994).
- [7] R. L. Marsa and M. W. Choptuik, Phys. Rev. D **54**, 4929 (1996).
- [8] First steps in this direction were taken by M. L. Gnedin and N. Y. Gnedin, Class. Quantum Grav. **10**, 1083 (1993) and by P. R. Brady and J. D. Smith, Phys. Rev. Lett. **75**, 1256 (1995).
- [9] M. W. Choptuik, Phys. Rev. Lett. **70**, 9 (1993).
- [10] R. S. Hamadé and J. M. Stewart, Class. Quantum Grav. **13**, 497 (1996).
- [11] See, e.g., C. Gundlach, Phys. Rev. D **55**, 695 (1997), and references cited therein.
- [12] C. Gundlach and J. Pullin, Class. Quantum Grav. **14**, 991 (1997).
- [13] E. Poisson and W. Israel, Phys. Rev. D **41**, 1796 (1990).
- [14] J. Bičák, Gen. Relativ. Gravitation **3**, 331 (1972).
- [15] The exact spherically-symmetric homothetic solution for the Einstein-scalar equations was first given by M. D. Roberts, Gen. Relativ. Gravitation **21**, 907 (1989). However, the solution given there in double-null coordinates is wrong. The correct solution in double-null coordinates was first derived by R. A. Sussman, J. Math. Phys. **32**, 223 (1991) and by Y. Oshiro, K. Nakamura, and A. Tomimatsu, Prog. Theor. Phys. **91**, 1265 (1994) and P. R. Brady, Class. Quantum Grav. **11**, 1255 (1994). See also L. M. Burko, Gen. Relativ. Gravitation **29**, 259 (1997).
- [16] This check was suggested to us by C. Gundlach, private communication.
- [17] For a table of QN mode frequencies see, e.g., S. Iyer, Phys. Rev. D **35**, 3632 (1987).
- [18] N. Andersson, Phys. Rev. D **55**, 468 (1997).